

# Identifying Key Descriptors for the Single-Atom Catalyzed CO Oxidation

Max J. Hülsey<sup>1</sup>, Sambath Baskaran<sup>2</sup>, Shipeng Ding<sup>1</sup>, Sikai Wang<sup>1,3</sup>, Hiroyuki Asakura<sup>4,5</sup>, Shinya Furukawa<sup>5,6</sup>, Shibo Xi<sup>7</sup>, Qi Yu<sup>8,9</sup>, Cong-Qiao Xu<sup>2</sup>, Jun Li<sup>2,9\*</sup> & Ning Yan<sup>1\*</sup>

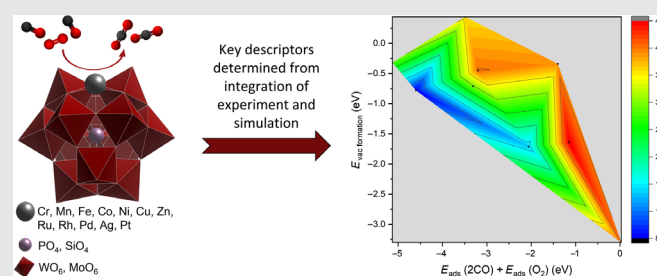
<sup>1</sup>Department of Chemical and Biomolecular Engineering, National University of Singapore, Singapore 117585, <sup>2</sup>Department of Chemistry, Southern University of Science and Technology, Shenzhen 518055, <sup>3</sup>Joint School of National University of Singapore, Tianjin University, International Campus of Tianjin University, Binhai New City, Fuzhou 350207, <sup>4</sup>Department of Molecular Engineering, Graduate School of Engineering, Kyoto University, Kyoto 615-8510; 615-8245, <sup>5</sup>Elements Strategy Initiative for Catalysts and Batteries (ESICB), Kyoto University, Kyoto 615-8245, <sup>6</sup>Institute for Catalysis, Hokkaido University, Sapporo 001-0021, <sup>7</sup>Institute for Chemical and Engineering Sciences, Agency for Science, Technology, and Research in Singapore, Singapore 138634, <sup>8</sup>Shaanxi Key Laboratory of Catalysis, Shaanxi University of Technology, Hangzhou 723001, <sup>9</sup>Department of Chemistry, Key Laboratory of Organic Optoelectronics and Molecular Engineering of Ministry of Education, Tsinghua University, Beijing 100084

\*Corresponding authors: [junli@tsinghua.edu.cn](mailto:junli@tsinghua.edu.cn); [ning.yan@nus.edu.sg](mailto:ning.yan@nus.edu.sg)

Cite this: CCS Chem. 2022, Just Published. DOI: 10.31635/ccschem.022.202201914

Fundamental knowledge of structure-activity correlations for heterogeneous single-atom catalysts (SACs) is essential in guiding catalytic design. While linear scaling relations are powerful for predicting the performance of traditional metal catalysts, they appear to fail with the involvement of SACs. Comparing the catalytic CO oxidation activity of different atomically dispersed metals (3d, 4d, and 5d) in conjunction with computational modeling enabled us to establish multiple scaling relations between the activity and simply calculated descriptors. Through these efforts, we found that the thermodynamic driving force for the oxygen vacancy formation needed to be considered in addition to the adsorption energies of substrates (in particular CO). Our approach was to reduce the computational requirements in determining better CO oxidation catalysts using a few key thermodynamic

descriptors. This work presents one of the first successful approaches for re-establishing scaling relations for catalytic reactions by SACs with potentially broad implications for catalytic processes actively involving this support.



**Keywords:** scaling relations, transition metals, carbon monoxide, single-site catalysts, polyoxometalate

## Introduction

The design of improved catalysts from the vast chemical space relies on the discovery of computationally inexpensive parameters that describe catalytic activity adequately.<sup>12</sup> Among others, scaling relationships linking properties like adsorption and reaction energies with activation

barriers have been developed for a range of reactions and surface morphologies but are so far predominantly focused on extended metal surfaces. While parameters like adsorption energies could be determined relatively quickly for large materials' libraries with high accuracy and precision, activation energies are significantly more challenging to calculate. For the case of CO oxidation on

extended fcc(111) surfaces and transition metal (TM) nanoparticles, linear correlations between the adsorption energies of O atoms, O<sub>2</sub>, and CO molecules, as well as the activation barriers, were predicted.<sup>3</sup> For nanoparticles supported on reducible oxides, the CO oxidation commonly follows a Mars-van Krevelen (MvK) mechanism with the support actively contributing to the catalytic reaction by donating and accepting O atoms. For this reason, the CO oxidation activity was found to correlate well with the reducibility of the support.<sup>4,5</sup> For metal oxides, scaling relations, in particular, for reactions involving C-H activation<sup>6-10</sup> had been assessed previously. However, parameters at the interface of metal species and oxide supports are rarely discussed, although they are known to be essential for heterogeneous catalysis and are present in virtually all industrial catalysts.<sup>11-14</sup>

Single-atom catalysts (SACs) have recently been shown to be active and selective for a variety of oxidation, reduction, and coupling reactions.<sup>15-28</sup> Density functional theory (DFT) calculations based on structures obtained via various tools such as X-ray absorption spectroscopy (XAS) serve as a powerful tool in revealing activity-structure correlations.<sup>15,16,27</sup> Although CO oxidation is among the earliest and most thoroughly investigated reactions, performed experimentally and by computational modeling,<sup>29-33</sup> clear guidelines for designing SACs are lacking. Obvious differences exist between catalytic surfaces and SACs because of the different electronic states, intimate metal-support interactions, the absence of adjacent TM atoms, and the absence of electronic bands forcing the treatment of scaling relations for SACs in alternative ways. In fact, many reports have shown that linear scaling relations do not apply to SACs supported on metal oxides or in host metals in so-called single-atom alloys.<sup>34-37</sup> This has been explained previously by the unique electronic structure of SACs,<sup>36,38</sup> geometric dynamics beyond what is achievable with nanoparticle catalysts,<sup>35</sup> and ensemble effects with host metals in the case of single-atom alloys.<sup>34,37</sup> Without discovering simple physical parameters of the catalysts governing catalytic activity, efficient screening of materials' libraries is severely prohibited by computational expenses.<sup>39</sup>

Herein, we describe the synthesis of Cr, Mn, Fe, Co, Ni, Cu, Zn, Ru, Rh, Pd, Ag, and Pt SACs supported by phosphomolybdic acid (PMA). We present evidence for atomic dispersion by XAS and CO diffuse reflectance infrared Fourier transform spectroscopy (DRIFTS), the uniform catalyst structure and morphology determined by N<sub>2</sub> sorption, scanning electron microscopy (SEM), Raman, and IR spectroscopies, as well as the determination of identical active site structural arrangement of the exposed four-fold hollow site surface area by all Keggin-structured polyoxometalates (POMs) (Figure 1).<sup>40,41</sup> Despite their structural similarities, the light-off temperatures for the CO oxidation reaction differed by as much as

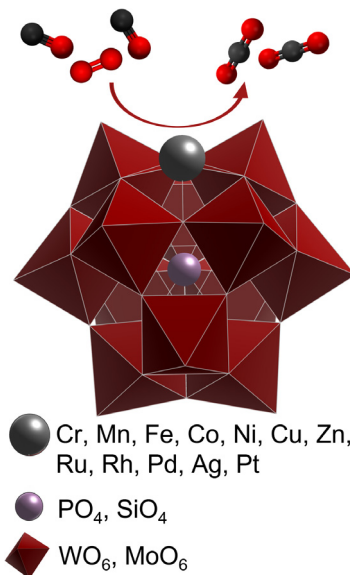


**Figure 1 |** Schematic depiction of the SACs investigated in this study. Different atomically dispersed TMs (Cr, Mn, Fe, Co, Ni, Cu, Zn, Ru, Rh, Pd, Ag, and Pt) are anchored on POMs composed of a central PO<sub>4</sub> unit with 12 surrounding edge-sharing MoO<sub>6</sub> units.

400 °C for the SACs. DFT calculations further confirmed the stability of the active site structure and the dominance of the MvK mechanism of the reaction kinetics. It was further used to predict the adsorption energies of the substrates and the product, along with the formation energy of the oxygen vacancy (O<sub>V</sub>). Scaling relations between each of the adsorption energies and the light-off temperatures did not well match the catalytic activity, but after including the O<sub>V</sub> formation energy, we understood the trends of the catalytic performance.

## Experimental Methods

### Catalyst synthesis and characterization

An aqueous solution of appropriate amounts of PMA in 30 mL of deionized water was cooled to 0 °C. Under stirring and cooling, a solution of 365 mg cesium nitrate (MilliporeSigma, Burlington, MA, USA) and the appropriate amount of chromium nitrate nonahydrate, manganese hydrate tetrahydrate, iron nitrate nonahydrate, cobalt nitrate hexahydrate, nickel nitrate hexahydrate, copper nitrate hemi(pentahydrate), zinc nitrate hexahydrate, ruthenium nitrosyl nitrate solution, rhodium nitrate, palladium nitrate dihydrate, and silver nitrate (all from MilliporeSigma, Burlington, MA, USA) dissolved in 30 mL deionized water with 5 drops of concentrated nitric acid was added gradually over 30 min period. The solution was aged for 5 h under constant stirring and ice cooling. The formed solid was then separated by

centrifugation (5 min, 8000 g) and washed twice with 30 mL of deionized water. After freeze-drying overnight, the catalysts were used as obtained.

Metal contents were determined using inductively coupled plasma-optical emission spectrometry (ICP-OES; iCAP 6000 series instrument; Thermo Fisher Scientific, Waltham, MA, USA) with calibration curves obtained from solutions with the pure metal salts. The catalysts were dissolved in aqua regia under heating at 80 °C for 4 h, and then the filtered solutions were diluted with an appropriate volume of deionized water before measurement. Attenuated total reflection (ATR-IR) spectroscopy was performed using a Thermo Scientific Nicolet iS50 FT-IR spectrometer (Thermo Fisher Scientific, Waltham, MA, USA) in the range of 525–4000 cm<sup>-1</sup> with a spectral resolution of 4 cm<sup>-1</sup>. Raman spectromicroscopy was performed using a Horiba Yvon Modular Raman spectrometer (Horiba, Kyoto, Japan) with a 532 nm excitation laser, 1% filter, a grating with 1200 mm<sup>-1</sup> and a  $\times 100$  objective. Calibration was done using the 521 cm<sup>-1</sup> vibrations of a silicon wafer. Field emission scanning electron microscopy (FESEM) was performed using a JEM-6700F (JEOL, Ltd., Tokyo, Japan) microscope.

## Computational modeling

Vienna Ab initio simulation package (VASP; version 5.3.5)<sup>42–44</sup> was used to perform spin-polarized DFT calculations. The projector augmented plane wave (PAW) pseudopotentials were employed to describe the electron-ion interaction.<sup>45</sup> The generalized gradient approximation (GGA) with the Perdew-Wang 91 (PW91) exchange-correlation functional was used,<sup>46</sup> and widely applied for single-atom supported polyoxometalate clusters by different research groups.<sup>47–49</sup> The plane wave cutoff energy was set to 400 eV in all calculations. A  $20 \times 20 \times 20 \text{ \AA}^3$  cubic box was used to avoid interactions between the periodic images, as reported by Macht et al.,<sup>47</sup> Yu et al.,<sup>48</sup> and Wang et al.<sup>49</sup> The  $\Gamma$  point was used for Brillouin zone center sampling. The total energy was converged to  $10^{-4}$  eV by applying the Gaussian smearing method with a width of 0.05 eV. All the ions were allowed to relax until the maximum atomic forces became less than 0.05 eV/ $\text{\AA}$ . The dimer method<sup>50–52</sup> was used to determine the transition states, followed by vibrational frequency calculations to confirm saddle points with one imaginary frequency.

Following the convention of thermodynamics, the adsorption energy ( $E_{\text{ads}}$ ) of O<sub>2</sub>, CO, or CO<sub>2</sub> on the TM@PMA surface was calculated as

$$E_{\text{ads}} = E_{\text{total}} - E_{\text{TM@PMA}} - E_{\text{adsorbate}}$$

where  $E_{\text{total}}$ ,  $E_{\text{TM@PMA}}$ , and  $E_{\text{adsorbate}}$  correspond to the electronic energies of adsorbed species on the TM@PMA, TM@PMA, and free adsorbates (CO, O<sub>2</sub>, and CO<sub>2</sub>), respectively.

The O<sub>v</sub> formation energy ( $E_{\text{vac formation}}$ ) of TM@PMA was calculated as

$$E_{\text{vac formation}} = -(E_{\text{CO-TM@PMA}} + E_{\text{CO}_2} - E_{\text{2CO-TM@PMA}})$$

where  $E_{\text{CO-TM@PMA}}$ ,  $E_{\text{CO}_2}$ , and  $E_{\text{2CO-TM@PMA}}$  correspond to the calculated electronic energies of adsorption structure with one CO molecule, gas-phase CO<sub>2</sub>, and adsorption structure with two CO molecules, respectively.

## CO DRIFTS

Approximately 100 mg catalyst powder was loaded in a Harricks HV-DR2 (Harrick Scientific Products Inc., Pleasantville, New York, United States) reaction cell covered by a Praying Mantis high-temperature reaction chamber with ZnS windows in a Thermo Scientific Nicolet iS50 FT-IR spectrometer; Thermo Fisher Scientific, Waltham, MA, USA) with a mercury-telluride (MCT) detector. The chamber was closed gastight, and background scans were recorded under 40 mL/min nitrogen gas flow (Air Liquide purity, 99.9995%) at room temperature. 40 mL/min 5% carbon monoxide in argon gas (Air Liquide) were introduced at 50 °C for 30 min, whereupon the diluted carbon monoxide gas flow was replaced with a gas flow of 40 mL/min nitrogen gas. During the gas treatments, spectra were collected regularly.

## CO oxidation reaction

For the CO oxidation reaction, appropriate amounts of the catalysts were loaded into a stainless-steel tubular plug flow reactor, fixed with quartz wool, and heated using a tube furnace with an external thermocouple. Before the reaction, catalysts were activated in a flow of 5% O<sub>2</sub> (balance Ar) for 60 min at 250 °C with a heating rate of 5 °C min<sup>-1</sup>. Then 2.5% CO and 2.5% O<sub>2</sub> (balance Ar) with a total flow rate of 80 mL min<sup>-1</sup> were introduced into the reactor set at room temperature. Subsequently, the temperatures were increased, and the reactor efflux was analyzed with an Agilent 7890B gas chromatograph (Agilent Technologies, Santa Clara, CA, USA) with a thermal conductivity (TCD) detector. Conversions and yields were determined after 30 min when a steady-state was reached.

## X-ray absorption spectroscopy

Self-supported undiluted pellets of 200 mg sample were pressed before measurements. X-ray absorption spectroscopy (XAS) measurements at the Cr, Mn, Fe, Co, Ni, and Cu K edges were performed using the X-ray absorption fine structure for catalysis (XAFCa) beamline detector at the Singapore Synchrotron Light Source (SSLS; Buona Vista, Singapore).<sup>53</sup> The storage ring of the SSLS was operated at 0.7 GeV with a maximum current of 200 mA. Data were collected at fluorescence mode while the respective metal

foils were measured in transmission mode simultaneously using a Si(111) double crystal monochromator. The average of 3–5 spectra was calculated to reduce noise. XAS measurements of the Ru, Rh, Pd-edges and Pt L<sub>3</sub>-edge were performed at BL37XU (Ru, Rh, Pd) and BL11XU (Pt) at SPring-8 (Japan Synchrotron Radiation Research Institute, Hyogo, Japan), operated at 8.0 GeV with a constant current of 99.5 mA. The XAS spectra were collected in fluorescence mode, while the standard samples were measured in transmission mode. For the Ru K-edge or Rh K-edge XAS measurement of the Ru/CsPMA or Rh/CsPMA, we exploited the fluorescence lines at Ru K $\beta$  or Rh K $\beta$  lines because the Mo K $\beta$  lines (19606 and 19962 eV) significantly overlapped with the Ru K $\alpha_1$  (19279 eV) or Rh K $\alpha_{1,2}$  lines (20216, 20074 eV), measured with a Ge solid-state detector (Mirion Technologies, Inc., Atlanta, GA, USA). For the Pd K-edge XAS measurement of Pd/CsPMA, we measured the XAS spectra typically using the Pd K $\alpha$  line. For the Pt L<sub>3</sub>-edge XAS measurement, we employed a high-energy resolution fluorescence detection (HERFD) method with a Si(733) spherically bent analyzer (XRS TECH LLC., Freehold, NJ, United States). The Pt L<sub>3</sub>-edge extended X-ray absorption spectroscopy (EXAFS) spectrum was broadened with a Gaussian function by 5 eV in width to make the EXAFS amplitude comparable to the EXAFS spectra measured in conventional transmission mode. We reported some of the details in a previous paper.<sup>54</sup> Data analysis was done with the Demeter software package.<sup>55</sup>  $\sigma^2$  values were determined from commercial metal oxide samples with a known crystal structure. X-ray absorption near-edge spectra (XANES) simulations were performed using the CASTEP ab initio quantum mechanical program code<sup>56</sup> with the PW91 exchange-correlation functional<sup>46</sup> based on the GGA. The plane-wave basis set was truncated at a kinetic energy of 400 eV. Wavelet transformation analysis was performed using the Morlet wavelet transform procedure with values for  $\kappa$  and  $\sigma$  of 5 and 1, respectively.<sup>57</sup>

## Results and Discussion

### Active site structure of M<sub>1</sub>/CsPMA

The single-atom M<sub>1</sub>/CsPMA catalysts were synthesized by a coprecipitation method starting with cesium nitrate, metal nitrate salts, and PMA, as reported previously.<sup>40,58</sup> Then the dried catalysts were used for analysis and catalytic testing without further modification. Atomic dispersion of the TMs was confirmed by XAS, as shown in Figure 2a. XANES revealed that all SACs were highly charged (2+, 3+, or 4+), and EXAFS confirmed that none of the catalysts exhibited metal-metal bond scattering, with all of them showing significant metal-oxygen scattering contributions (Figure 2b, Table 1, Supporting Information Table S1, and Figures S1–S10). EXAFS fitting was consistent with the formation of the active site,

which displayed metal atoms in the four-fold hollow sites of the Keggin structure with adsorption of one O<sub>2</sub> molecule, except for Cu<sub>1</sub>/CsPMA and Pd<sub>1</sub>/CsPMA, which showed no adsorbed O<sub>2</sub>. This was consistent with DFT calculated O<sub>2</sub> adsorption energies (vide infra). For 4d elements, the XAS analysis was more complicated due to the strong X-ray fluorescence of Mo close to the absorption edges of Ru, Rh, and Pd. Nevertheless, Morlet wavelet transformation analysis suggested that the SAC only exhibited first shell coordination to light scattering atoms like oxygen and none to heavier atoms like TMs (Figure 2c and Supporting Information Figures S11–S19). To develop an appropriate catalyst model for atomistic simulations, we ensured that all the catalysts exhibited the same known active site structure. XANES simulations based on DFT-calculated catalyst structures could help identify the exact local coordination environment. Metal oxide samples were used as a reference to confirm the validity of the employed level of theory (Supporting Information Figure S20). For the predicted active site structures, an almost ideal overlap between simulated and experimental spectra confirmed the formation of active site structures, as discussed above (Figure 2d and Supporting Information Figure S20). This is in accordance with our previous findings, where the active sites of POM-supported Rh<sub>1</sub> and Pd<sub>1</sub> catalysts were elucidated in detail.<sup>58,59</sup>

We employed the DRIFTS technique as another approach to confirm the single-atom identity using CO as a probe molecule. We observed that even CsPMA without additional metal adsorbs CO with two broad vibration bands at 1930, 2042 and a sharper one at 2122 cm<sup>−1</sup>, probably assignable to O-CO and Mo-CO species. None of the SACs based on early TMs showed additional CO adsorption bands, which was in line with their generally low CO affinity; another possible explanation might be the lower extinction coefficient of CO adsorbed on undercoordinated or charged metal sites such as those presented by our SACs.<sup>60</sup> For some of the heavier elements, however, strong CO adsorption could be observed, in particular, for Rh, Ag, and Pt. For Rh<sub>1</sub>/CsPMA, two CO molecules were adsorbed simultaneously, and both the symmetric and asymmetric vibrations were visible at 2027 and 2099 cm<sup>−1</sup>, similar to previous reports on Rh SACs.<sup>58,61</sup> Ag<sub>1</sub>/CsPMA adsorbs CO with an IR vibration at 2182 cm<sup>−1</sup>, slightly higher than gas-phase CO, indicating the presence of a non-classical carbonyl as commonly observed for cationic closed-shell d<sup>10</sup> systems like Ag<sup>+</sup>.<sup>62</sup> In the CO DRIFT spectrum of Pt<sub>1</sub>/CsPMA, a dominant peak at 2122 cm<sup>−1</sup> was observed, indicative of a highly positively charged Pt in a 4+ oxidation state. A shoulder at 2099 cm<sup>−1</sup> was probably related to Pt<sup>2+</sup> species.<sup>32,63,64</sup> Furthermore, no additional peaks in the range of 1750–2080 cm<sup>−1</sup> were observed, suggesting the absence of metallic nanoparticles in all the catalysts (Figure 3).<sup>63,65</sup> A summary of approximate oxidation

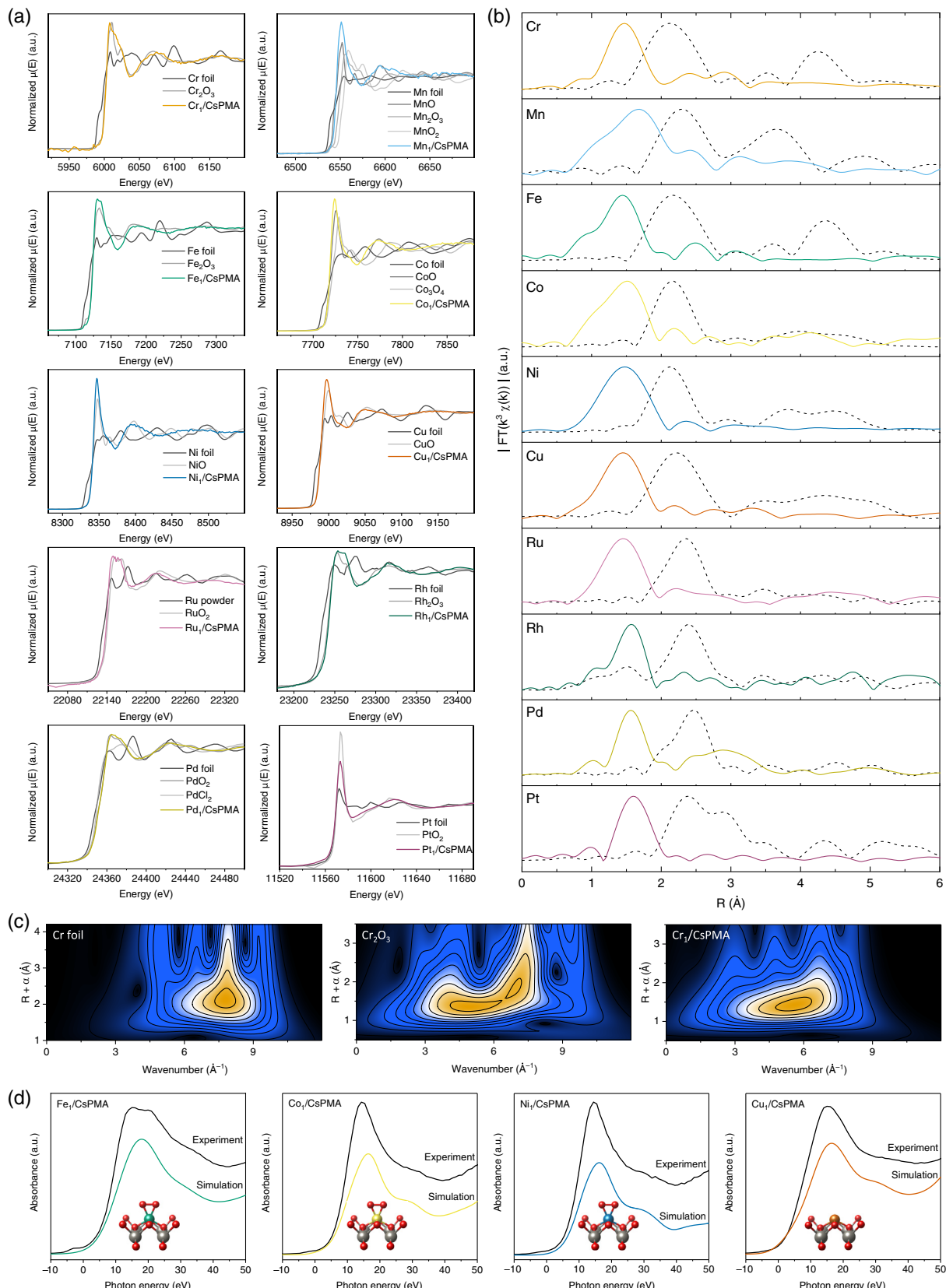


**Figure 2 | Confirmation of the SAC structure of  $M_1/CsPMA$ .** (a)  $K$  edge XANES spectra of ten different  $M_1/CsPMA$  catalysts and their respective metallic and oxide reference materials. (b)  $R$ -space EXAFS spectra of different  $M_1/CsPMA$  catalysts (colored, solid lines) and their respective metal foils (black, dashed lines). (c) Morlet wavelet transformation analysis of Cr foil,  $Cr_2O_3$ , and  $Cr_1/CsPMA$ . (d) Experimental and simulated XANES spectra for different  $M_1/CsPMA$  catalysts; the active site structure considered for XANES simulations are shown. Additional data are shown in the supporting information.

**Citation:** CCS Chem. 2022, Just Published. DOI: [10.31635/ccschem.022.202201914](https://doi.org/10.31635/ccschem.022.202201914)

**Link to VoR:** <https://doi.org/10.31635/ccschem.022.202201914>

**Table 1 | EXAFS Fitting Parameters of Some Representative  $M_1/CsPMA$  Materials. Additional Details Can Be Found in the Supporting Information**

	Coordination Shell	CN	R (Å)	$\sigma^2$
CoO	Co-O	6	$2.10 \pm 0.04$	$0.017 \pm 0.008$
Co <sub>1</sub> /CsPMA		$6.0 \pm 1.9$	$2.03 \pm 0.04$	$0.009 \pm 0.007$
Rh <sub>2</sub> O <sub>3</sub>	Rh-O	6	$2.04 \pm 0.01$	$0.003 \pm 0.001$
Rh <sub>1</sub> /CsPMA		$6.8 \pm 0.9$	$2.02 \pm 0.01$	$0.003 \pm 0.002$
PtO <sub>2</sub>	Pt-O	6	$2.14 \pm 0.02$	$0.001 \pm 0.002$
Pt <sub>1</sub> /CsPMA		$3.9 \pm 0.7$	$2.13 \pm 0.01$	$0.001 \pm 0.002$

states for the different  $M_1/CsPMA$  catalysts based on CO DRIFTS and XANES is provided in Table 2.

For the electrostatic stabilization of SACs, the POM structure must be preserved during the synthesis and catalytic reaction. The stability and persistence of the Keggin structure after the adsorption of TMs were confirmed by Raman and infrared spectroscopies. For both CsPMA and the  $M_1/CsPMA$  materials, the vibrational modes typical for PMA were apparent, whereas no overlap existed with the spectrum of MoO<sub>3</sub> or other molybdenum oxides (Figures 4a and 4b).<sup>66</sup> The surface areas determined ranged from 89–132 m<sup>2</sup> g<sup>-1</sup> by N<sub>2</sub> physisorption and Brunauer–Emmett–Teller (BET) analysis. Those values were typical for precipitated POMs and were not

significantly affected by the type of atomically dispersed metal. FESEM images of the different  $M_1/CsPMA$  catalysts showed a consistent morphology featuring spherical particles predominantly, with radii between 100–300 nm (Figure 4c and Supporting Information Figure S21). At higher magnification, the surface of those particles appeared to be rough with features a few nanometers in size (Supporting Information Figure S22).

### Scaling relations for the CO oxidation activity of $M_1/CsPMA$

CO oxidation light-off curves were measured with a plug-flow reactor at temperatures up to 500 °C. When the T<sub>20</sub> temperatures for the CO oxidation reaction were compared on different SACs, significant differences were visible, especially between earlier TMs, some of which exhibited T<sub>20</sub> values above 400 °C, identified as noble metals. Rh constituted the most active SAC with a T<sub>20</sub> value of ~88 °C, followed by Pd, Pt, and Ru with T<sub>20</sub> values of 173, 244, and 308 °C, respectively (Figure 5a). The differences were much less pronounced for earlier TMs, although Co SACs appeared to be particularly active for CO oxidation with a T<sub>20</sub> temperature of 330 °C, almost paralleling Ru<sub>1</sub>/CsPMA. Other metals analyzed were Cr, Mn, Cu, Fe, Zn, and Ni, with T<sub>20</sub> values of 382, 413, 425, 430, 465, and 466 °C, respectively. Ag<sub>1</sub>/CsPMA appeared to be a special case where the coordination of CO in the non-classical carbonyl seemed to have inhibited the background activity of the support (Supporting Information Figure S23). As the T<sub>20</sub> value exceeded 500 °C, the Ag-based SAC was omitted from further analysis of scaling relations. Raman and IR spectroscopy confirmed the stability of the catalyst support after the reaction had reached up to 500 °C (Supporting Information Figure S24). This is in accordance with our previous studies in which the stability of the POM-supported Rh SACs at high reaction temperatures was demonstrated.<sup>58,67</sup>

In order to correlate the catalytic CO oxidation activity with simple physicochemical properties of the SACs, we carried out DFT calculations on PMA-supported TM. To confirm the validity of the catalyst model used for

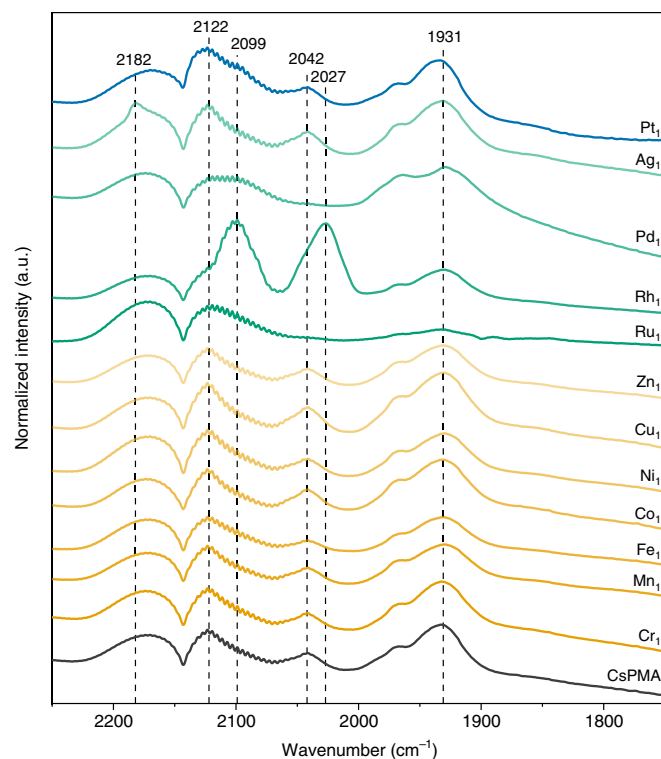


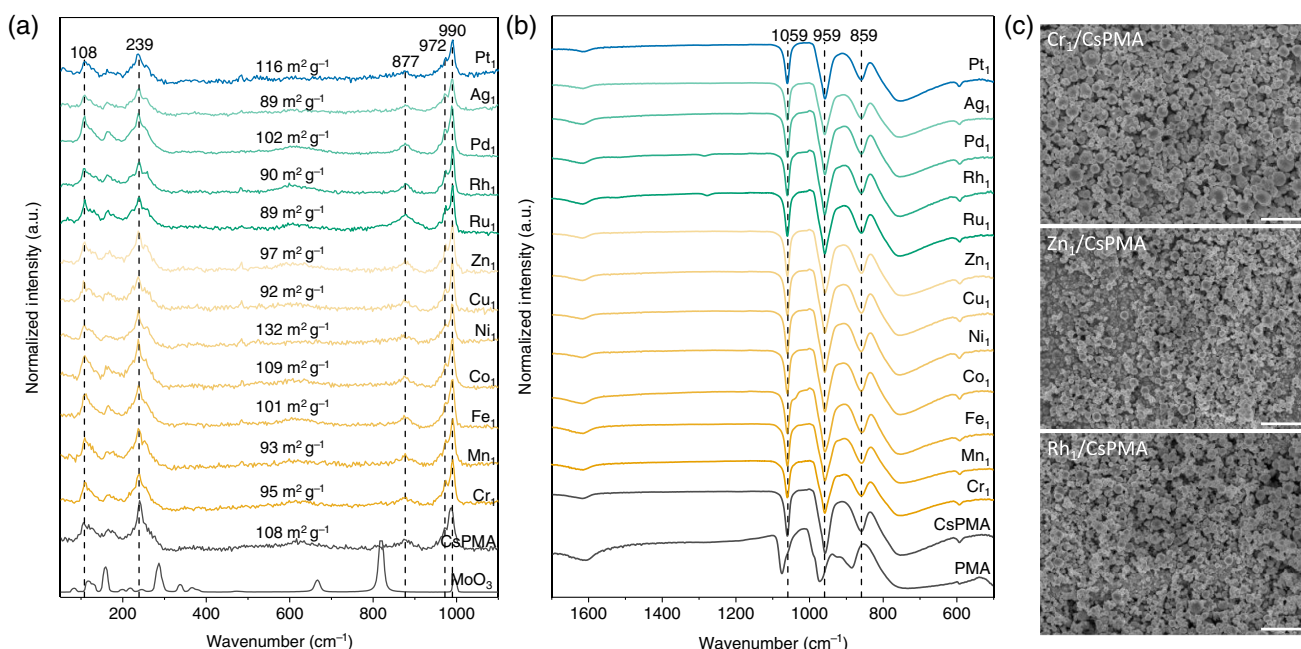
**Figure 3 | CO DRIFTS spectra for CsPMA and different  $M_1/CsPMA$  catalysts under a 5% CO atmosphere.**

**Table 2 | Approximate Oxidation State of  $M_1/CsPMA$  Materials Based on CO DRIFTS and XAS**

	Cr	Mn	Fe	Co	Ni	Cu	Ru	Rh	Pd	Ag	Pt
Oxidation state based on CO DRIFTS	N.D.	3+	N.D.	1+	4+/2+						
Oxidation state based on EXAFS	3+	2+	3+	2+	2+	2+	4+	3+	2+	N.D.	2+

the simulations, analyses of the assumed reaction mechanism for  $Rh_1/CsPMA$  were also performed. The predicted mechanism matched the MvK mechanism previously determined by spectroscopic and kinetic analyses with support reoxidation as a rate-determining step (Supporting Information Figures S23a and S23b).<sup>58</sup> We expected other SACs to have other reaction barriers or rate-determining steps. For high-throughput computational screening of catalyst materials, it was beneficial to identify simple thermodynamic parameters that could be determined with minimum computational efforts. Often, scaling relationships are established by correlating between adsorption energies of different substrates and the activity. SACs were naturally different from extended metal surfaces because they did not possess adjacent metal active sites; thus, coverage effects and lateral interactions between adsorbates did not play a role. Furthermore, metal centers in SACs interacted solely with the support, highlighting the importance of considering the participation of the support during the catalytic reaction in modeling. Screening of the adsorption energies of CO and O<sub>2</sub> (Supporting

Information Table S2 and Figure S25) on all TM revealed clear trends throughout the periodic table (Supporting Information Figure S26). Generally, trends among different rows were comparable with slightly larger adsorption energies for heavier TMs due to increased *nd* orbital radii. Stark differences were evident when groups of TMs with low CO but high O<sub>2</sub> binding energies were compared in groups 3–6; generally, low adsorption energies for both substrates in groups 10–12 and balanced O<sub>2</sub> adsorption strength coupled with high CO adsorption energies in groups 7–9. The formation of oxygen vacancies was endothermic for groups 3–7 (except Mn) and then monotonously increased in energy up to group 11 but was slightly less favorable for group 12. From these trends, it became obvious that early TMs were too oxophilic, preventing the O<sub>V</sub> formation and hampering CO adsorption, while late TMs did not bind CO strongly, and their high O<sub>V</sub> formation energies likely led to thermodynamically unbalanced reaction energy profiles. It appeared that only catalysts with balanced adsorption strengths and O<sub>V</sub> formation energies were effective in the oxidation of CO (Figure 5b and

**Figure 4 | Characterization of the POM structure and morphology of  $M_1/CsPMA$ . (a) Raman spectra of  $M_1/CsPMA$  with labels of the surface areas determined by BET analysis of N<sub>2</sub> adsorption isotherms, (b) Infrared spectra of  $M_1/CsPMA$ , (c) FESEM images of different catalysts; the scale bar has a length of 2  $\mu$ m.**

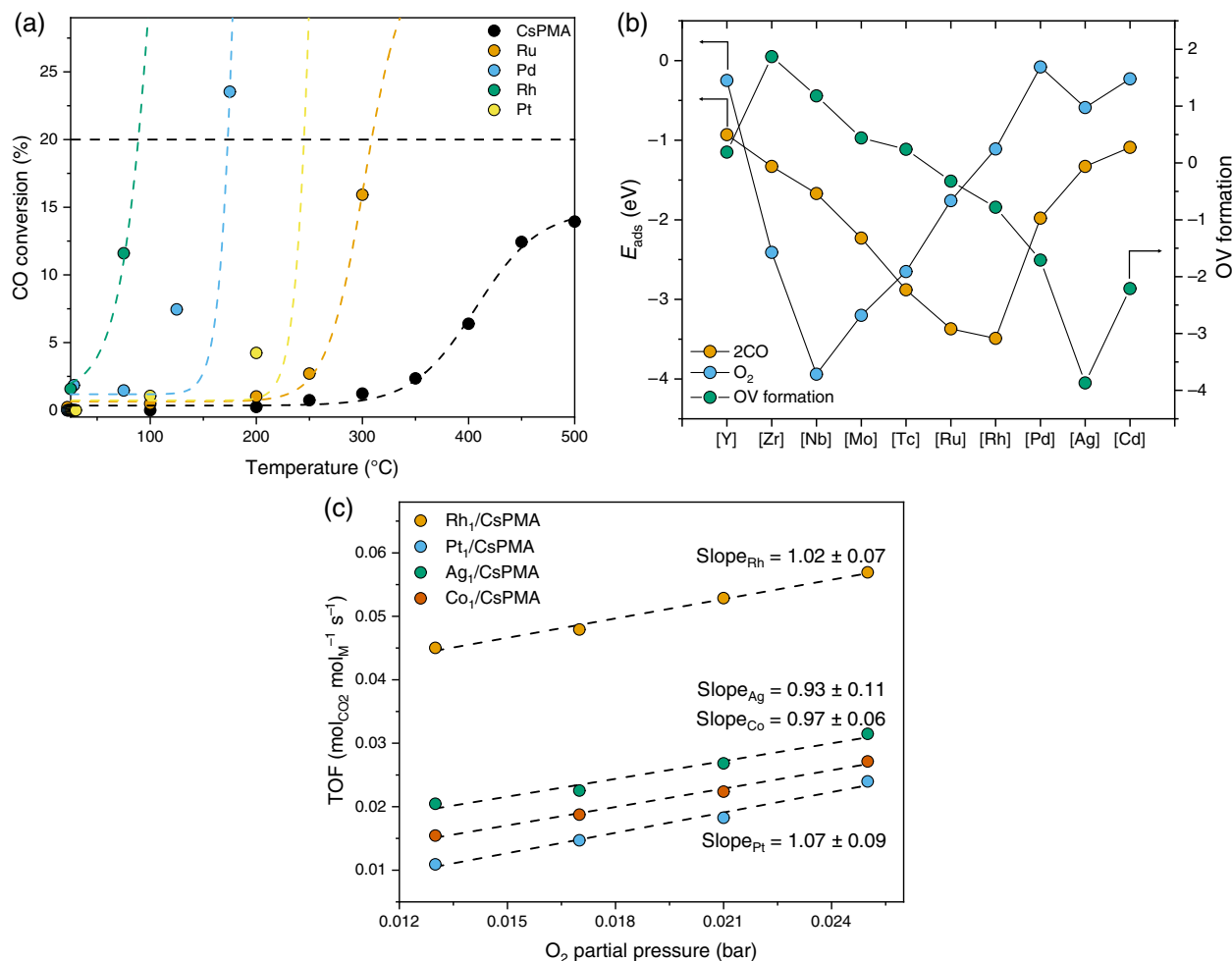


**Figure 5 |** CO oxidation activity and reaction descriptors of different  $M_1/\text{CsPMA}$  catalysts. (a) Light-off curves of select  $M_1/\text{CsPMA}$  catalysts (see *Supporting Information Figure S23* for additional catalysts). The horizontal line at 20% CO conversion serves to guide the eye. (b) Calculated CO and  $\text{O}_2$  adsorption and  $\text{O}_v$  formation energies on  $M_1/\text{CsPMA}$  ( $M = 4\text{d TM}$ ). The more stable of the two different  $\text{O}_2$  adsorption modes ( $\text{O}_{2,s} \eta^2$  side-on, and  $\text{O}_{2,e} \eta^1$  end-on) were considered. (c)  $\text{O}_2$  reaction order for different  $M_1/\text{CsPMA}$  catalysts at different temperatures.

*Supporting Information Figure S26*). Although  $\text{O}_2$  adsorption occurred in the oxygen vacant metal-support interface in the MvK mechanism, we found that these adsorption energies were almost congruent with those on the metal site alone (*Supporting Information Figure S27*). Therefore, we decided to rely on the  $\text{O}_2$  adsorption energies on the vacancy-free metal sites as the more readily accessible parameter.

To verify if all the PMA-based SACs followed the same mechanism, we measured the reaction orders towards  $\text{O}_2$  for different catalysts. There appeared to be a linear correlation between the  $\text{O}_2$  partial pressure and the reaction rate, suggesting that the reaction order was 1 towards the oxidant (Figure 5c). Since the orders were comparable for  $\text{Co}_1/\text{CsPMA}$ ,  $\text{Rh}_1/\text{CsPMA}$ ,  $\text{Ag}_1/\text{CsPMA}$ , and  $\text{Pt}_1/\text{CsPMA}$ , our hypothesis of an MvK mechanism across different SAC active sites appeared valid. In particular, for easily reducible supports, oxygen vacancies

were most commonly suggested to be involved in the mechanism of single-atom catalyzed (CO) oxidation reactions.

Among the 3d and 4d elements, group 9 metals supported on PMA yielded the best CO oxidation catalysts. Although they possessed the highest CO adsorption energies, this parameter alone was not adequate for predicting the catalytic activity (*Supporting Information Figure S28a*). Also, neither the sum of the adsorption energies of reactants (CO and  $\text{O}_2$ ) nor the  $\text{O}_v$  formation alone provided good guidelines to predict catalyst performance (*Supporting Information Figures S28b* and *S28c*). Overall, none of the 1D scaling relationships between the  $T_{20}$  values and the thermodynamic parameters yielded good correlations, indicating that they were insufficient to determine reactivity, contrary to what was reported in most previous studies on nanoparticle or nanocluster catalysts.<sup>68</sup> The active contribution of the

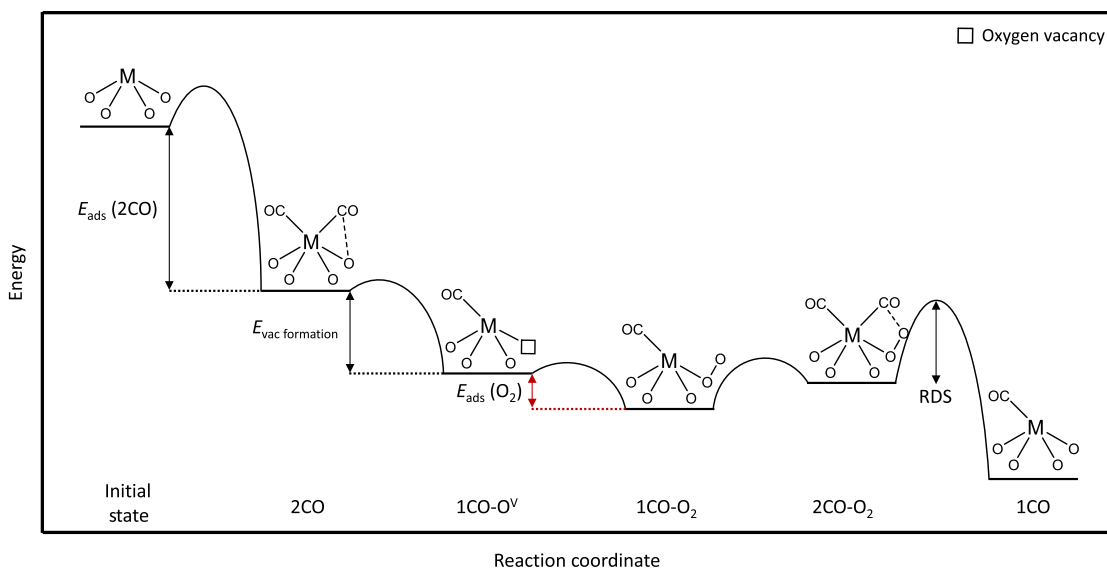


**Figure 6 |** Reaction energy diagram of the single-atom catalyzed CO oxidation following an MvK mechanism; the thermodynamic predators for activity are highlighted (a proxy is used for the  $\text{O}_2$  adsorption energy shown in red).

support in an MvK mechanism could be attributable to the physical parameters determining activity.

Since oxygen vacancies are an integral part of the MvK mechanism, we examined the importance of adsorption energies of the substrates and the thermodynamics of the  $\text{O}^{\vee}$  formation. For the reaction mechanism, the initial adsorption of CO, the formation of an  $\text{O}^{\vee}$ , and the adsorption of  $\text{O}_2$  were crucial in achieving a catalytic turnover. All these steps needed to have suitable reaction energies that were neither too high nor too low to yield a balanced energy profile (Figure 6). Therefore, we deduced that the 2D scaling relations were solely based on the DFT-calculated reaction energies alongside the experimental  $T_{20}$  values yielded a more complete picture (Figure 7). It was apparent that if the  $\text{O}^{\vee}$  formation or the substrate binding was endothermic, the catalyst performance would be poor. In the case of strong adsorbate binding, the  $\text{O}^{\vee}$  formation energy could be comparably lower without compromising activity, and this compensation effect between both factors allowed for a larger ‘region’ of good CO oxidation performance. While care must be taken not to overinterpret the findings here to other reaction mechanisms such as the Langmuir-Hinshelwood (LH) or Eley-Rideal (ER) mechanisms, certain generalizations could be inferred. Without the contribution of oxygen vacancies to the reaction mechanism, the adsorption energies of CO and  $\text{O}_2$  became the sole thermodynamic descriptors of catalytic reactivity. The LH-type mechanisms requiring the co-adsorption of both reactants would benefit from strong but relatively similar binding energies. Those requirements would mostly be fulfilled by group 7, group 11, and group 12 metals. Although we did not find AgI/CsPMA to follow a distinct pathway compared to other materials, this might

be due to the large oxygen vacancy formation energies favoring the MvK mechanism. ER mechanisms are mainly proposed to rely on the reaction of gas-phase  $\text{O}_2$  with two adsorbed CO molecules, which would mean that

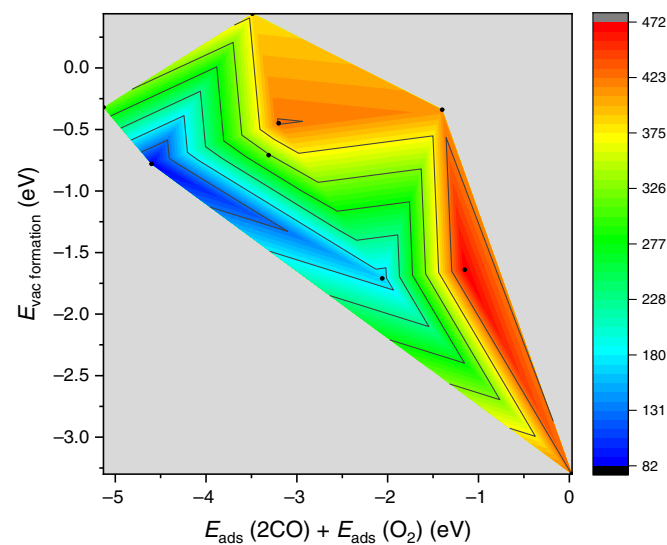


**Figure 7 |** 2D scaling relations derived from experiments in conjunction with the DFT-calculated sum of the adsorption energies of two CO molecules and one  $\text{O}_2$  molecule (in the more favorable adsorption mode) and the  $\text{O}^{\vee}$  formation energy. Experimental  $T_{20}$  values with the respective DFT-calculated energies are plotted as black dots. Uncertainty exists about the behavior of the  $T_{20}$  values in the grey area. In particular, the area in the left bottom corner (high  $E_{\text{vac formation}}$  and strong substrate adsorption) remains elusive.

materials with adsorption energies of CO above that of O<sub>2</sub> and relatively low oxygen vacancy formation energies might be beneficial. In our simulations, this would only be the case for Sc, Y, and to a much lesser extent, Mn and Tc. None of the calculated descriptors here could serve as reasonable proxies for the barriers to the reaction of two adsorbed CO molecules with O<sub>2</sub> from the gas phase; therefore, conclusions on ER energetics should be substantiated by systematic studies on catalysts that follow LH- or ER-type mechanisms.

## Conclusion

This study provides an example to correlate experimental activity data with DFT-derived thermodynamic properties of known catalytic active site structures. By considering the O<sub>V</sub> formation energy, we understood the catalytic performance and provided further guidelines for SACs improvement. Due to the dominant role of metal-support interaction in determining the active site properties, SACs are suitable model catalysts to investigate how metal sites and the support act synergistically in a systematic fashion. Beyond CO oxidation, the contribution of oxygen vacancies has been reported for a variety of reactions such as the oxidation of CH<sub>4</sub>,<sup>69</sup> hydrodeoxygenation,<sup>70-72</sup> as well as several photo- and electrochemical reactions.<sup>73,74</sup> We envision that the methodology developed here would aid the rational design of improved catalysts for a wide variety of reactions. Other catalysts comprising close interactions between metal structures and supports (such as the three-atom single-cluster catalyst of M<sub>3</sub>/graphydinie<sup>75</sup>) and reactions that actively involve support might benefit from this approach.

## Supporting Information

Supporting Information is available and includes the details of the XAS fitting, wavelet transformation analysis, additional XANES simulations, FESEM images, CO oxidation light-off curves, additional DFT calculations, and scaling relations (PDF). Details for the computational methods are attached in a separate document.

## Conflict of Interest

There is no conflict of interest to report.

## Acknowledgments

The authors thank the National University of Singapore (NUS) Flagship Green Energy Program (grant nos. R-279-000-553-646 and R-279-000-553-731) and the National Natural Science Foundation of China (grant nos.

92061109, 22033005, and 22038002) for their financial support. N.Y. and J.L. thank the Asian Universities Alliance (AUA) Scholars Award for the sponsorship. Q.Y. acknowledges the hospitality of NUS and Tsinghua University during her sabbatical visit. This work was partially sponsored by the Guangdong Provincial Key Laboratory of Catalysis (grant no. 2020B121201002) and the Natural Science Basic Research Program of Shaanxi (2021JCW-20 and S2020-JC-WT-0001). Computational resources were supported by the Center for Computational Science and Engineering (SUSTech) and Tsinghua National Laboratory for Information Science and Technology.

## References

1. Toyao, T.; Maeno, Z.; Takakusagi, S.; Kamachi, T.; Takigawa, I.; Shimizu, K.-I. Machine Learning for Catalysis Informatics: Recent Applications and Prospects. *ACS Catal.* **2020**, *10*, 2260-2297.
2. Liu, X.; Xiao, J.; Peng, H.; Hong, X.; Chan, K.; Nørskov, J. K. Understanding Trends in Electrochemical Carbon Dioxide Reduction Rates. *Nat. Commun.* **2017**, *8*, 15438.
3. Falsig, H.; Hvolbæk, B.; Kristensen, I. S.; Jiang, T.; Bligaard, T.; Christensen, C. H.; Nørskov, J. K. Trends in the Catalytic CO Oxidation Activity of Nanoparticles. *Angew. Chem. Int. Ed.* **2008**, *47*, 4835-4839.
4. Widmann, D.; Behm, R. J. Active Oxygen on an Au/TiO<sub>2</sub> Catalyst: Formation, Stability, and CO Oxidation Activity. *Angew. Chem. Int. Ed.* **2011**, *50*, 10241-10245.
5. Schlexer, P.; Widmann, D.; Behm, R. J.; Pacchioni, G. CO Oxidation on an Au/TiO<sub>2</sub> Nanoparticle Catalyst via the Au-Assisted Mars-van Krevelen Mechanism. *ACS Catal.* **2018**, *8*, 6513-6525.
6. Kumar, G.; Lau, S. L. J.; Krcha, M. D.; Janik, M. J. Correlation of Methane Activation and Oxide Catalyst Reducibility and Its Implications for Oxidative Coupling. *ACS Catal.* **2016**, *6*, 1812-1821.
7. Fung, V.; Tao, F. F.; Jiang, D.-E. General Structure-Reactivity Relationship for Oxygen on Transition-Metal Oxides. *J. Phys. Chem. Lett.* **2017**, *8*, 2206-2211.
8. Aljama, H.; Nørskov, J. K.; Abild-Pedersen, F. Theoretical Insights into Methane C-H Bond Activation on Alkaline Metal Oxides. *J. Phys. Chem. C* **2017**, *121*, 16440-16446.
9. Fung, V.; Polo-Garzon, F.; Wu, Z.; Jiang, D.-E. Exploring Perovskites for Methane Activation from First Principles. *Catal. Sci. Technol.* **2018**, *8*, 702-709.
10. Latimer, A. A.; Kulkarni, A. R.; Aljama, H.; Montoya, J. H.; Yoo, J. S.; Tsai, C.; Abild-Pedersen, F.; Studt, F.; Nørskov, J. K. Understanding Trends in C-H Bond Activation in Heterogeneous Catalysis. *Nat. Mater.* **2017**, *16*, 225-229.
11. Gao, W.; Hood, Z. D.; Chi, M. Interfaces in Heterogeneous Catalysts: Advancing Mechanistic Understanding through Atomic-Scale Measurements. *Acc. Chem. Res.* **2017**, *50*, 787-795.
12. Xie, C.; Niu, Z.; Kim, D.; Li, M.; Yang, P. Surface and Interface Control in Nanoparticle Catalysis. *Chem. Rev.* **2020**, *120*, 1184-1249.

13. Huang, W.; Li, W.-X. Surface and Interface Design for Heterogeneous Catalysis. *Phys. Chem. Chem. Phys.* **2019**, *21*, 523–536.
14. Xie, Z.; Tian, D.; Xie, M.; Yang, S.-Z.; Xu, Y.; Rui, N.; Lee, J. H.; Senanayake, S. D.; Li, K.; Wang, H.; Kattel, S.; Chen, J. G. Interfacial Active Sites for CO<sub>2</sub> Assisted Selective Cleavage of C-C/C-H Bonds in Ethane. *Chem.* **2020**, *6*, 2703–2716.
15. Yang, X.-F.; Wang, A.; Qiao, B.; Li, J.; Liu, J.; Zhang, T. Single-Atom Catalysts: A New Frontier in Heterogeneous Catalysis. *Acc. Chem. Res.* **2013**, *46*, 1740–1748.
16. Liu, P.; Zhao, Y.; Qin, R.; Mo, S.; Chen, G.; Gu, L.; Chevrier, D. M.; Zhang, P.; Guo, Q.; Zang, D.; Wu, B.; Fu, G.; Zheng, N. Photochemical Route for Synthesizing Atomically Dispersed Palladium Catalysts. *Science* **2016**, *352*, 797.
17. Lin, L.; Zhou, W.; Gao, R.; Yao, S.; Zhang, X.; Xu, W.; Zheng, S.; Jiang, Z.; Yu, Q.; Li, Y.-W.; Shi, C.; Wen, X.-D.; Ma, D. Low-Temperature Hydrogen Production from Water and Methanol Using Pt/α-MoC Catalysts. *Nature* **2017**, *544*, 80–83.
18. Hülsey, M. J.; Zhang, J.; Yan, N. Harnessing the Wisdom in Colloidal Chemistry to Make Stable Single-Atom Catalysts. *Adv. Mater.* **2018**, *30*, 1802304.
19. Wang, A.; Li, J.; Zhang, T. Heterogeneous Single-Atom Catalysis. *Nat. Rev. Chem.* **2018**, *2*, 65–81.
20. Liu, J.-C.; Tang, Y.; Wang, Y.-G.; Zhang, T.; Li, J. Theoretical Understanding of the Stability of Single-Atom Catalysts. *Natl. Sci. Rev.* **2018**, *5*, 638–641.
21. Ding, S.; Hülsey, M. J.; Pérez-Ramírez, J.; Yan, N. Transforming Energy with Single-Atom Catalysts. *Joule* **2019**, *3*, 2897–2929.
22. Cao, S.; Yang, M.; Elnabawy, A. O.; Trimpalis, A.; Li, S.; Wang, C.; Göltl, F.; Chen, Z.; Liu, J.; Shan, J.; Li, M.; Haas, T.; Chapman, K. W.; Lee, S.; Allard, L. F.; Mavrikakis, M.; Flytzani-Stephanopoulos, M. Single-Atom Gold Oxo-Clusters Prepared in Alkaline Solutions Catalyse the Heterogeneous Methanol Self-Coupling Reactions. *Nat. Chem.* **2019**, *11*, 1098–1105.
23. Ding, S.; Guo, Y.; Hülsey, M. J.; Zhang, B.; Asakura, H.; Liu, L.; Han, Y.; Gao, M.; Hasegawa, J.-Y.; Qiao, B.; Zhang, T.; Yan, N. Electrostatic Stabilization of Single-Atom Catalysts by Ionic Liquids. *Chem* **2019**, *5*, 3207–3219.
24. Zhuo, H.-Y.; Zhang, X.; Liang, J.-X.; Yu, Q.; Xiao, H.; Li, J. Theoretical Understandings of Graphene-Based Metal Single-Atom Catalysts: Stability and Catalytic Performance. *Chem. Rev.* **2020**, *120*, 12315–12341.
25. Liu, J.; Zou, Y.; Cruz, D.; Savateev, A.; Antonietti, M.; Vilé, G. Ligand–Metal Charge Transfer Induced via Adjustment of Textural Properties Controls the Performance of Single-Atom Catalysts during Photocatalytic Degradation. *ACS Appl. Mater. Interfaces* **2021**, *13*, 25858–25867.
26. Zhang, X.; Zhang, M.; Deng, Y.; Xu, M.; Artiglia, L.; Wen, W.; Gao, R.; Chen, B.; Yao, S.; Zhang, X.; Peng, M.; Yan, J.; Li, A.; Jiang, Z.; Gao, X.; Cao, S.; Yang, C.; Kropf, A. J.; Shi, J.; Xie, J.; Bi, M.; van Bokhoven, J. A.; Li, Y.-W.; Wen, X.; Flytzani-Stephanopoulos, M.; Shi, C.; Zhou, W.; Ma, D. A Stable Low-Temperature H<sub>2</sub>-Production Catalyst by Crowding Pt on α-MoC. *Nature* **2021**, *589*, 396–401.
27. Vilé, G.; Di Liberto, G.; Tosoni, S.; Sivo, A.; Ruta, V.; Nachtegaal, M.; Clark, A. H.; Agnoli, S.; Zou, Y.; Savateev, A.; Antonietti, M.; Pacchioni, G. Azide-Alkyne Click Chemistry over a Heterogeneous Copper-Based Single-Atom Catalyst. *ACS Catal.* **2022**, *12*, 2947–2958.
28. Li, S.; Cao, R.; Xu, M.; Deng, Y.; Lin, L.; Yao, S.; Liang, X.; Peng, M.; Gao, Z.; Ge, Y.; Liu, J.-X.; Li, W.-X.; Zhou, W.; Ma, D. Atomically Dispersed Ir/α-MoC Catalyst with High Metal Loading and Thermal Stability for Water-Promoted Hydrogenation Reaction. *Natl. Sci. Rev.* **2022**, *9*, nwab026.
29. Qiao, B.; Wang, A.; Yang, X.; Allard, L. F.; Jiang, Z.; Cui, Y.; Liu, J.; Li, J.; Zhang, T. Single-Atom Catalysis of CO Oxidation Using Pt<sub>1</sub>/FeO<sub>x</sub>. *Nat. Chem.* **2011**, *3*, 634–641.
30. Moses-DeBusk, M.; Yoon, M.; Allard, L. F.; Mullins, D. R.; Wu, Z.; Yang, X.; Veith, G.; Stocks, G. M.; Narula, C. K. CO Oxidation on Supported Single Pt Atoms: Experimental and ab Initio Density Functional Studies of CO Interaction with Pt Atom on 0-Al<sub>2</sub>O<sub>3</sub>(010) Surface. *J. Am. Chem. Soc.* **2013**, *135*, 12634–12645.
31. Jones, J.; Xiong, H.; DeLaRiva, A. T.; Peterson, E. J.; Pham, H.; Challa, S. R.; Qi, G.; Oh, S.; Wiebenga, M. H.; Pereira Hernández, X. I.; Wang, Y.; Datye, A. K. Thermally Stable Single-Atom Platinum-on-Ceria Catalysts via Atom Trapping. *Science* **2016**, *353*, 150–154.
32. Nie, L.; Mei, D.; Xiong, H.; Peng, B.; Ren, Z.; Hernandez, X. I. P.; DeLaRiva, A.; Wang, M.; Engelhard, M. H.; Kovarik, L.; Datye, A. K.; Wang, Y. Activation of Surface Lattice Oxygen in Single-Atom Pt/CeO<sub>2</sub> for Low-Temperature CO Oxidation. *Science* **2017**, *358*, 1419–1423.
33. Sarma, B. B.; Plessow, P. N.; Agostini, G.; Concepción, P.; Pfänder, N.; Kang, L.; Wang, F. R.; Studt, F.; Prieto, G. Metal-Specific Reactivity in Single-Atom Catalysts: CO Oxidation on 4d and 5d Transition Metals Atomically Dispersed on MgO. *J. Am. Chem. Soc.* **2020**, *142*, 14890–14902.
34. Darby, M. T.; Stamatakis, M.; Michaelides, A.; Sykes, E. C. H. Lonely Atoms with Special Gifts: Breaking Linear Scaling Relationships in Heterogeneous Catalysis with Single-Atom Alloys. *J. Phys. Chem. Lett.* **2018**, *9*, 5636–5646.
35. Gani, T. Z. H.; Kulik, H. J. Understanding and Breaking Scaling Relations in Single-Site Catalysis: Methane to Methanol Conversion by Fe<sup>IV</sup>=O. *ACS Catal.* **2018**, *8*, 975–986.
36. Greiner, M. T.; Jones, T. E.; Beeg, S.; Zwiener, L.; Scherzer, M.; Girgsdies, F.; Piccinin, S.; Armbrüster, M.; Knop-Gericke, A.; Schlögl, R. Free-Atom-Like d States in Single-Atom Alloy Catalysts. *Nat. Chem.* **2018**, *10*, 1008–1015.
37. Sun, G.; Zhao, Z.-J.; Mu, R.; Zha, S.; Li, L.; Chen, S.; Zang, K.; Luo, J.; Li, Z.; Purdy, S. C.; Kropf, A. J.; Miller, J. T.; Zeng, L.; Gong, J. Breaking the Scaling Relationship via Thermally Stable Pt/Cu Single Atom Alloys for Catalytic Dehydrogenation. *Nat. Commun.* **2018**, *9*, 4454.
38. Tao, H.; Choi, C.; Ding, L.-X.; Jiang, Z.; Han, Z.; Jia, M.; Fan, Q.; Gao, Y.; Wang, H.; Robertson, A. W.; Hong, S.; Jung, Y.; Liu, S.; Sun, Z. Nitrogen Fixation by Ru Single-Atom Electrocatalytic Reduction. *Chem* **2019**, *5*, 204–214.
39. Esterhuizen, J. A.; Goldsmith, B. R.; Linic, S. Theory-Guided Machine Learning Finds Geometric Structure-Property Relationships for Chemisorption on Subsurface Alloys. *Chem* **2020**, *6*, 3100–3117.

40. Zhang, B.; Asakura, H.; Zhang, J.; Zhang, J.; De, S.; Yan, N. Stabilizing a Platinum Single-Atom Catalyst on Supported Phosphomolybdic Acid without Compromising Hydrogenation Activity. *Angew. Chem. Int. Ed.* **2016**, *55*, 8319–8323.
41. Zhang, B.; Sun, G.; Ding, S.; Asakura, H.; Zhang, J.; Sautet, P.; Yan, N. Atomically Dispersed Pt<sub>1</sub>-Polyoxometalate Catalysts: How Does Metal-Support Interaction Affect Stability and Hydrogenation Activity? *J. Am. Chem. Soc.* **2019**, *141*, 8185–8197.
42. Kresse, G.; Furthmüller, J. Efficiency of Ab-Initio Total Energy Calculations for Metals and Semiconductors Using a Plane-Wave Basis Set. *Comput. Mater. Sci.* **1996**, *6*, 15–50.
43. Kresse, G.; Hafner, J. Ab Initio Molecular-Dynamics Simulation of the Liquid-Metal-Amorphous-Semiconductor Transition in Germanium. *Phys. Rev. B: Condens. Matter Mater. Phys.* **1994**, *49*, 14251–14269.
44. Kresse, G.; Hafner, J. Ab Initio Molecular Dynamics for Liquid Metals. *Phys. Rev. B: Condens. Matter Mater. Phys.* **1993**, *47*, 558–561.
45. Blöchl, P. E. Projector Augmented-Wave Method. *Phys. Rev. B: Condens. Matter Mater. Phys.* **1994**, *50*, 17953–17979.
46. Perdew, J. P.; Wang, Y. Accurate and Simple Analytic Representation of the Electron-Gas Correlation Energy. *Phys. Rev. B: Condens. Matter Mater. Phys.* **1992**, *45*, 13244–13249.
47. Macht, J.; Janik, M. J.; Neurock, M.; Iglesia, E. Catalytic Consequences of Composition in Polyoxometalate Clusters with Keggin Structure. *Angew. Chem. Int. Ed.* **2007**, *46*, 7864–7868.
48. Yu, M.-A.; Feng, Y.; Gao, L.; Lin, S. Phosphomolybdic Acid Supported Single-Metal-Atom Catalysis in CO Oxidation: First-Principles Calculations. *Phys. Chem. Chem. Phys.* **2018**, *20*, 20661–20668.
49. Wang, S.; Feng, Y.; Lin, S.; Guo, H. Phosphomolybdic Acid Supported Atomically Dispersed Transition Metal Atoms (M = Fe, Co, Ni, Cu, Ru, Rh, Pd, Ag, Os, Ir, Pt, and Au): Stable Single Atom Catalysts Studied by Density Functional Theory. *RSC Adv.* **2017**, *7*, 24925–24932.
50. Henkelman, G.; Jónsson, H. A Dimer Method for Finding Saddle Points on High Dimensional Potential Surfaces Using Only First Derivatives. *J. Chem. Phys.* **1999**, *111*, 7010–7022.
51. Heyden, A.; Bell, A. T.; Keil, F. J. Efficient Methods for Finding Transition States in Chemical Reactions: Comparison of Improved Dimer Method and Partitioned Rational Function Optimization Method. *J. Chem. Phys.* **2005**, *123*, 224101.
52. Kästner, J.; Sherwood, P. Superlinearly Converging Dimer Method for Transition State Search. *J. Chem. Phys.* **2008**, *128*, 014106.
53. Du, Y.; Zhu, Y.; Xi, S.; Yang, P.; Moser, H. O.; Breese, M. B. H.; Borgna, A. XAFCA: A New XAFS Beamline for Catalysis Research. *J. Synchrotron Radiat.* **2015**, *22*, 839–843.
54. Asakura, H.; Kawamura, N.; Mizumaki, M.; Nitta, K.; Ishii, K.; Hosokawa, S.; Teramura, K.; Tanaka, T. A Feasibility Study of “Range-Extended” EXAFS Measurement at the Pt L<sub>3</sub>-Edge of Pt/Al<sub>2</sub>O<sub>3</sub> in the Presence of Au<sub>2</sub>O<sub>3</sub>. *J. Anal. At. Spectrom.* **2018**, *33*, 84–89.
55. Ravel, B.; Newville, M., ATHENA, ARTEMIS, HEPHAESTUS: Data Analysis for X-Ray Absorption Spectroscopy Using IFEFFIT. *J. Synchrotron Radiat.* **2005**, *12*, 537–541.
56. Segall, M. D.; Lindan, P. J. D.; Probert, M. J.; Pickard, C. J.; Hasnip, P. J.; Clark, S. J.; Payne, M. C. First-Principles Simulation: Ideas, Illustrations and the CASTEP Code. *J. Phys. Condens. Matter* **2002**, *14*, 2717–2744.
57. Funke, H.; Scheinost, A. C.; Chukalina, M. Wavelet Analysis of Extended X-Ray Absorption Fine Structure Data. *Phys. Rev. B* **2005**, *71*, 094110.
58. Hülsey, M. J.; Zhang, B.; Ma, Z.; Asakura, H.; Do, D. A.; Chen, W.; Tanaka, T.; Zhang, P.; Wu, Z.; Yan, N. In Situ Spectroscopy-Guided Engineering of Rhodium Single-Atom Catalysts for CO Oxidation. *Nat. Commun.* **2019**, *10*, 1330.
59. Hülsey, M. J.; Geng, S.; Bin, Z.; Yao, X.; Shipeng, D.; Sie Shing, W.; Ying, Z.; Shinya, F.; Hiroyuki, A.; Yongqiang, C.; Zili, W.; Rui, S.; Ding, M.; Philippe, S.; Ning, Y. Zero-Valent Pd Atoms Anchored on Polyoxometalate for Low Temperature Hydrodeoxygenation. *ChemRxiv* **2020**.
60. Lansford, J. L.; Vlachos, D. G. Infrared Spectroscopy Data- and Physics-Driven Machine Learning for Characterizing Surface Microstructure of Complex Materials. *Nat. Commun.* **2020**, *11*, 1513.
61. Lang, R.; Li, T.; Matsumura, D.; Miao, S.; Ren, Y.; Cui, Y.-T.; Tan, Y.; Qiao, B.; Li, L.; Wang, A.; Wang, X.; Zhang, T. Hydroformylation of Olefins by a Rhodium Single-Atom Catalyst with Activity Comparable to RhCl(PPh<sub>3</sub>)<sub>3</sub>. *Angew. Chem. Int. Ed.* **2016**, *55*, 16054–16058.
62. Hurlburt, P. K.; Rack, J. J.; Luck, J. S.; Dec, S. F.; Webb, J. D.; Anderson, O. P.; Strauss, S. H. Nonclassical Metal Carbonyls: [Ag(CO)]<sup>+</sup> and [Ag(CO)<sub>2</sub>]<sup>+</sup>. *J. Am. Chem. Soc.* **1994**, *116*, 10003–10014.
63. DeRita, L.; Dai, S.; Lopez-Zepeda, K.; Pham, N.; Graham, G. W.; Pan, X.; Christopher, P. Catalyst Architecture for Stable Single Atom Dispersion Enables Site-Specific Spectroscopic and Reactivity Measurements of CO Adsorbed to Pt Atoms, Oxidized Pt Clusters, and Metallic Pt Clusters on TiO<sub>2</sub>. *J. Am. Chem. Soc.* **2017**, *139*, 14150–14165.
64. Zhang, Z.; Zhu, Y.; Asakura, H.; Zhang, B.; Zhang, J.; Zhou, M.; Han, Y.; Tanaka, T.; Wang, A.; Zhang, T.; Yan, N. Thermally Stable Single Atom Pt/m-Al<sub>2</sub>O<sub>3</sub> for Selective Hydrogenation and CO Oxidation. *Nat. Commun.* **2017**, *8*, 16100.
65. Wang, H.; Liu, J.-X.; Allard, L. F.; Lee, S.; Liu, J.; Li, H.; Wang, J.; Wang, J.; Oh, S. H.; Li, W.; Flytzani-Stephanopoulos, M.; Shen, M.; Goldsmith, B. R.; Yang, M. Surpassing the Single-Atom Catalytic Activity Limit through Paired Pt-O-Pt Ensemble Built from Isolated Pt<sub>1</sub> Atoms. *Nat. Commun.* **2019**, *10*, 3808.
66. Dieterle, M.; Weinberg, G.; Mestl, G. Raman Spectroscopy of Molybdenum Oxides Part I. Structural Characterization of Oxygen Defects in MoO<sub>3-x</sub> by DR UV/VIS, Raman Spectroscopy and X-Ray Diffraction. *Phys. Chem. Chem. Phys.* **2002**, *4*, 812–821.
67. Zhang, B.; Asakura, H.; Yan, N. Atomically Dispersed Rhodium on Self-Assembled Phosphotungstic Acid:

- Structural Features and Catalytic CO Oxidation Properties. *Ind. Eng. Chem. Res.* **2017**, *56*, 3578–3587.
68. Liu, J.-X.; Su, Y.; Filot, I. A. W.; Hensen, E. J. M. A Linear Scaling Relation for CO Oxidation on CeO<sub>2</sub>-Supported Pd. *J. Am. Chem. Soc.* **2018**, *140*, 4580–4587.
69. Fujimoto, K.-I.; Ribeiro, F. H.; Avalos-Borja, M.; Iglesia, E. Structure and Reactivity of PdO<sub>x</sub>/ZrO<sub>2</sub> Catalysts for Methane Oxidation at Low Temperatures. *J. Catal.* **1998**, *179*, 431–442.
70. Goulas, K. A.; Mironenko, A. V.; Jenness, G. R.; Mazal, T.; Vlachos, D. G. Fundamentals of C–O Bond Activation on Metal Oxide Catalysts. *Nat. Catal.* **2019**, *2*, 269–276.
71. Mironenko, A. V.; Vlachos, D. G. Conjugation-Driven “Reverse Mars–van Krevelen”-Type Radical Mechanism for Low-Temperature C–O Bond Activation. *J. Am. Chem. Soc.* **2016**, *138*, 8104–8113.
72. Fu, J.; Lym, J.; Zheng, W.; Alexopoulos, K.; Mironenko, A. V.; Li, N.; Boscoboinik, J. A.; Su, D.; Weber, R. T.; Vlachos, D. G. C–O Bond Activation Using Ultralow Loading of Noble Metal Catalysts on Moderately Reducible Oxides. *Nat. Catal.* **2020**, *3*, 446–453.
73. Crumlin, E. J.; Mutoro, E.; Liu, Z.; Grass, M. E.; Biegalski, M. D.; Lee, Y.-L.; Morgan, D.; Christen, H. M.; Bluhm, H.; Shao-Horn, Y. Surface Strontium Enrichment on Highly Active Perovskites for Oxygen Electrocatalysis in Solid Oxide Fuel Cells. *Energy Environ. Sci.* **2012**, *5*, 6081–6088.
74. Asahi, R.; Morikawa, T.; Ohwaki, T.; Aoki, K.; Taga, Y. Visible-Light Photocatalysis in Nitrogen-Doped Titanium Oxides. *Science* **2001**, *293*, 269–271.
75. Liu, J.-C.; Xiao, H.; Zhao, X.-K.; Zhang, N.-N.; Liu, Y.; Xing, D.-H.; Yu, X.-H.; Hu, H.-S.; Li, J. Computational Prediction of Graphdiyne-Supported Three-Atom Single-Cluster Catalysts. *CCS Chem.* **2022**. doi:<https://doi.org/10.31635/ccschem.022.202201914>